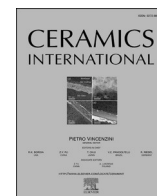




Contents lists available at ScienceDirect

Ceramics International

journal homepage: www.elsevier.com/locate/ceramint

Piezoelectric responses of PVDF-KBT electrospun nanocomposite fibres via nanoscale mapping

Van Dang Tran^{a,*}, Hong-Cuong Truong^a, Thanh Vinh Nguyen^a, Philippe Leclère^b,
Thanh-Tung Duong^a, Thi Hang Bui^a, Van Quy Nguyen^a

^a International Training Institute for Materials Science, Hanoi University of Science and Technology, No.1, Dai Co Viet Street, Hai Ba Trung, Hanoi, Viet Nam

^b Laboratory for Physics of Nanomaterials and Energy, Research Institute in Materials Science and Engineering, University of Mons (UMONS), B-7000, Mons, Belgium

ARTICLE INFO

Handling Editor: Dr P. Vincenzini

Keywords:

PVDF-KBT
PFM
Nano-Raman
Nanocomposite fibers
Piezoelectric generator

ABSTRACT

The piezoelectric properties of polyvinylidene fluoride (PVDF) and $K_{0.5}Bi_{0.5}TiO_3$ (KBT) electrospun composite nanofibers were studied in view of their application for Piezoelectric generator (PEG) devices. The orientation of the polar β -phase throughout the PVDF/KBT nanofibers was investigated at the nanoscale, revealing a maximum β -phase content of 67%. Remarkably enhanced piezoelectric responses were observed in the PVDF-KBT composite, supported by comprehensive analyses including local hysteresis loops piezoresponse mapping and advanced mapping AFM-based techniques. The PVDF/KBT nanofiber-based PEG demonstrated consistent performance, with an output voltage of 16 V, a current of $0.85 \mu A/cm^2$, and a power density of $13.6 \mu W/cm^2$ at $10^7 \Omega$, showcasing its potential as a sustainable energy solution with the ability to recharge portable electronic devices.

1. Introduction

The energy crisis, exacerbated by the conflict in Ukraine, has underscored the imperative of transitioning to alternative energy sources. Dependence on conventional fossil fuels and their adverse environmental effects has raised mounting concerns, necessitating the substitution of cleaner and more sustainable energy sources, including thermal, wind, vibrational, and solar energy [1]. On the other hand, advancements in technology have facilitated the miniaturisation of electronic devices and the integration of energy-efficient technologies. This progress has paved the way for the development of low-power systems that can function with minimal energy consumption. Consequently, mechanical energy harvesting offers significant potential for powering low-power sensor networks and wearable electronics [2]. Vibrational mechanical energy, abundantly available in our surroundings, can be effectively converted into electrical energy through the direct piezoelectric effect by employing piezoelectric generators [3]. Therefore, piezoelectric harvesters based on piezoelectric materials have received considerable attention in recent years due to their simple structure, which makes them easy to integrate with sensors and other electronic devices [4]. The piezoelectric materials themselves play a vital role as a crucial component in a piezoelectric energy harvester,

exerting a significant influence on the output performance of a PEG device. The piezoelectric and mechanical properties of the piezoelectric layer in a PEG are essential for achieving optimal performance and energy conversion efficiency [5]. The piezoelectric charge coefficient, also referred to as the d coefficient, serves as a measure of the piezoelectric response. A high piezoelectric charge coefficient ensures a greater energy harvesting capacity from the same mechanical input. Moreover, the piezoelectric layer must effectively respond to mechanical vibrations and deformations during operation. Therefore, the mechanical flexibility of the layer stands as a critical factor in ensuring the generation of a stable output [6]. Piezoelectric materials can be classified into two categories: ceramics and polymers. Ceramic materials have been widely used in piezoelectric energy harvesting due to their excellent piezoelectric charge coefficients [7–10]. However, their brittleness and processing difficulties limit their suitability for flexible and cost-effective applications. Conversely, polymer-based piezoelectric materials, including PVDF and its copolymers, have gained attention for their lightweight nature, mechanical flexibility, and biocompatibility. Nonetheless, their lower piezoelectric charge coefficients result in reduced output voltage, which constrains their use in PEG applications [11–13]. In an effort to overcome these limitations, researchers have attempted to combine ceramic and polymer piezoelectric materials to create a

* Corresponding author.

E-mail address: dang.tranvan@hust.edu.vn (V.D. Tran).

<https://doi.org/10.1016/j.ceramint.2023.09.161>

Received 19 July 2023; Received in revised form 13 September 2023; Accepted 14 September 2023

Available online 20 September 2023

0272-8842/© 2023 Elsevier Ltd and Techna Group S.r.l. All rights reserved.

composite with improved piezoelectric properties and mechanical stability [14]. The addition of ceramic nanoparticles as fillers in a PVDF polymer matrix can have a significant effect on their piezoelectrical and mechanical properties. PVDFs' piezoelectric properties mainly stem from their polar crystalline phases, namely the β -phase (TTTT conformation) and γ phase (T3GT3G' conformation), rather than the nonpolar α -phase (TG' conformation) [15]. The β -phase, with its larger spontaneous polarisation, exhibits the highest piezoelectric response. The overall piezoelectric behaviour of PVDF is influenced by the quantity and crystallisation of the β phase, as well as the level of crystallinity. Nanofillers, such as organically modified nanoclays, functionalised carbon nanotubes, metal nanoparticles, and graphene and its derivatives are used to enhance the content of the β -phase and stabilise β -phase nanocrystals by leveraging their specific interactions [16–20]. The incorporation of nanofillers facilitates the formation of aligned PVDF chains at additional interfaces, contributing to improved orientation and properties.

In this work, we developed and characterised, in terms of piezoelectric coefficient, the mechanical stability and electrical performance of a novel PEG which is based on electrospun PVDF-KBT nanocomposite fibres. The nanoparticle piezoelectric $K_{0.5}Bi_{0.5}TiO_3$ (KBT) ceramics with a uniform size were fabricated via the hydrothermal method. KBT ceramic was chosen for its lead-free composition and environmentally friendly nature, in addition to its high piezoelectric coefficients and low dielectric loss that have been reported [21–23]. It was believed that adding KBT nanoparticles would enhance the crystallisation of PVDF and achieve high β -phase content. Two electrodes, aluminium foil and a platinum coating on PET were put on the two sides of the composite fibre film to develop a flexible piezoelectric energy harvester with the desired toughness. The effect of KBT nanoparticles on crystallinity and the nanomechanical and piezoelectric properties of composite nanofibers was evaluated in detail at nanoscale through the AFM technique. As a result of the optimisation conditions, the piezoelectric energy harvester achieved a peak output power density of $13.6 \mu W/cm^2$. It has the capability to charge capacitors, power LEDs, and supply electronic devices. Additionally, the innovative design allows for its application as a force or motion sensor. These research findings provide valuable insights into optimising the piezoelectric properties for improved output performance in advanced composite-based piezoelectric energy harvesters utilising electrospun nanofibers.

2. Material and methods

2.1. Synthesis of KBT nanoparticles

The KBT nanoparticles were synthesised via a hydrothermal process, in which bismuth nitrate and titanium oxide were reacted in a 15 M KOH solution at a temperature of 220 °C. The mixture was mechanically stirred and then placed in a stainless-steel autoclave for 12 h. Following the completion of the reaction, the autoclave was cooled down to room temperature. Then, the collected powder was rinsed with DI water and subjected to annealing at 700 °C for 4 h.

2.2. Electrospinning of PVDF/KBT nanocomposite fibres

A solution was prepared by mixing 0.58 g of PVDF powder (Mw \approx 375,000 g/mol, Sigma-Aldrich) with a solvent mixture of 4 ml acetone and 6 ml DMF. KBT nanoparticles, synthesised via a hydrothermal process, were finely milled and added to the PVDF solution at varying concentrations (0, 2, 5, 7, 10, and 15 wt%). The mixture was stirred for 8 h at 70 °C. Electrospinning of the PVDF/KBT solution was conducted using a TL-Pro automated electrospinning instrument equipped with a 500 μ m inner diameter steel needle. During electrospinning, a voltage of 12 kV was applied at the metal needle and -2 kV at the collector, while the solution was continuously supplied to the needle tip at a consistent rate of 0.5 ml/h. The resulting nanocomposite fibres were collected on a

rolling drum positioned 10 cm from the needle under ambient conditions with a temperature of 25 °C and a relative humidity of 40%. For characterisation purposes, the nanocomposite fibres were deposited onto three different types of substrates: glass substrates for examining morphology, crystallinity, and nanoscale mechanical properties, ITO-conductive substrates for investigating piezoelectric properties, and Pt/PET substrates for fabricating PEG devices.

2.3. Fabrication of PEG devices

As mentioned above, a platinum film with a thickness of 200 nm was deposited onto a polyethylene terephthalate (PET) substrate via the sputtering method, using it as a PEG bottom electrode. The Pt/PET electrode was fixed onto an electrospinning roller to collect the electrospun fibres. The PVDF/KBT film was optimised with a thickness of $\sim 5 \mu$ m and coated on Pt/PET, then dried at 110 °C for 2 h in the oven. After the annealing process, a layer of polydimethylsiloxane (PDMS) was spin-coated onto the side of the electrode covered with composite fibres. This resulted in the formation of a PDMS film that filled the gaps between the nanofibers, providing structural stability and protecting the piezoelectric fibres. Subsequently, aluminium foil, as the top electrode, was adhered to the PDMS layer and cured at 70 °C for 1 h. The samples were then covered using antistatic tape to complete the PEG.

2.4. Characterizations

The composite fibre morphology was analysed by SEM (Jeol instrument). XRD patterns were obtained using a Multi-purpose X-ray diffractometer (Rigaku-SmartLab XE). One-dimensional thin film XRD was conducted using Cu-K α X-ray radiation (wavelength: 1.5418 Å) with a goniometer omega/2 θ setup. The diffraction angle 2 θ ranged from 10° to 70°, incrementing by 0.0262606°/min, and a scan speed of 15 s was employed. A zero-background holder (ZBH) made of single-crystal silicon was utilised to minimise XRD background originating from diffraction and incoherent scattering linked to the sample holder. The peak deconvolution routine was applied to calculate the total degree of crystallinity (DoC, ϕ_{total}) and β -crystallinity (ϕ_{β}) of the composite films using SmartLab Studio II software. This software separates XRD data into amorphous and crystalline contributions using curve fitting. The process combines the fitted amorphous profile from Fourier-series fitting with peaks representing the crystalline contribution, described by a Voigt peak function. Upon completing the deconvolution, the software calculates the total degree of crystallinity and β -crystallinity by comparing the area under the Voigt peaks to the total area under all peaks, including the amorphous contribution. The following equations were used to quantify the crystallinity of α and β/γ phases separately:

$$DoC = \frac{\sum A_{crys}}{\sum A_{crys} + \sum A_{amr}} \times 100 \% \quad (2.1)$$

$$B_{crys} = \frac{\sum A_{\beta}}{\sum A_{\alpha} + \sum A_{\beta} + \sum A_{\gamma}} \times DoC, (i = \alpha, \beta, \gamma) \quad (2.2)$$

Where $\sum A_{crys}$ and $\sum A_{amr}$ are the summation of the integral area of the crystalline peaks and the amorphous halo from PVDF, respectively. $\sum A_{\alpha}$, $\sum A_{\beta}$, and $\sum A_{\gamma}$ indicate the total integral area from α , β , and γ -phase peaks, respectively.

Raman mapping spectra were acquired using a Horiba-LabRAM Nano system equipped with AFM-correlated nano-Raman spectroscopy. Surface-enhanced Raman scattering (SERS) measurements were performed using a 532 nm argon ion laser as the excitation source, with a power range of 100 nW to 1 mW, on a diffraction-limited spot of approximately 300 nm on the surface of the composite fibre.

The local piezoelectric response of PVDF/KBT nanofibers was investigated using PFM switching spectroscopy (SS-PFM) using an atomic force microscope (Dimension Icon from Bruker). A conductive

probe with a Pt/Ir-coated silicon tip and cantilever (PPP-EFM, Nanosensors), possessing a stiffness of approximately 3.5 N/m, was employed in the experiment. Peak Force Quantitative Nanomechanical Mapping (PFQNM) was employed to assess the mechanical properties of the composite fibre and to detect the area which embedded the KBT particles. To ensure accurate force application to the sample, calibration steps were used to determine the spring constant of the cantilever and the deflection sensitivity. The local piezoresponse force microscopy measurement was conducted using the SS-PFM, which has been reported [24]. The contact resonance frequency was determined based on the highest amplitude response, and a sweeping DC bias of 30 V was applied for polarisation switching as a poling step. Hysteresis loops were obtained from different zones on the nanofibers using SS-PFM, with an AC bias of 3 V in the DART mode applied to the conductive AFM tip. The same procedure was repeated two times at each selected point. The second data acquisition cycle was collected for analysis, and the maximum butterfly loop value represented the piezoresponse (PR) amplitude.

The output performance of the PEG was evaluated by subjecting the device to an external force applied perpendicular to its surface using a specially designed mechanical pushing machine and recording the output with a digital oscilloscope (Rigol-MSO8104) and an electrometer (high resistance meter-Keysight -B2985B). In order to analyse the energy storage performance characteristics of the piezoelectric energy harvester, an AC-to-DC conversion was performed using a full bridge

rectifier circuit. This allowed for analysing parameters such as energy storage efficiency, charging capacity, and the ability to deliver a stable DC output.

3. Results and discussion

3.1. PVDF/KBT composite fibre characterisations

The optimal doping content was determined using scanning electron microscopy (SEM), as presented in Fig. 1. Fig. 1a–f depict the morphological changes of the electrospun composite fibres at varying doping levels of KBT (0%, 2%, 5%, 7%, 10% and 15%). Additional information is provided in Supplementary Fig. S1a, which displays the SEM of the hydrothermally synthesised KBT nanoparticles, showcasing their morphology and particle sizes. These ceramic particles exhibit diverse shapes, such as spheres, squares, and hexagons, with sizes distributed in the range of 50–150 nm. Fig. 1a shows the pristine PVDF fibres which appear smooth with no discernible particles on the surface. In contrast, Fig. 1b displays the 2% doping PVDF/KBT fibres, where nanoparticles are visibly diffused in the nano fibres. This observation suggests the success of the doping process and the effective incorporation of nanoparticles into the PVDF fibres. Such a structure is anticipated to synergistically enhance load distribution and bolster the mechanical properties of the composite. Fig. 1c and d correspond to the 5% and 7% KBT doping levels in PVDF/KBT fibres, respectively. The increasing

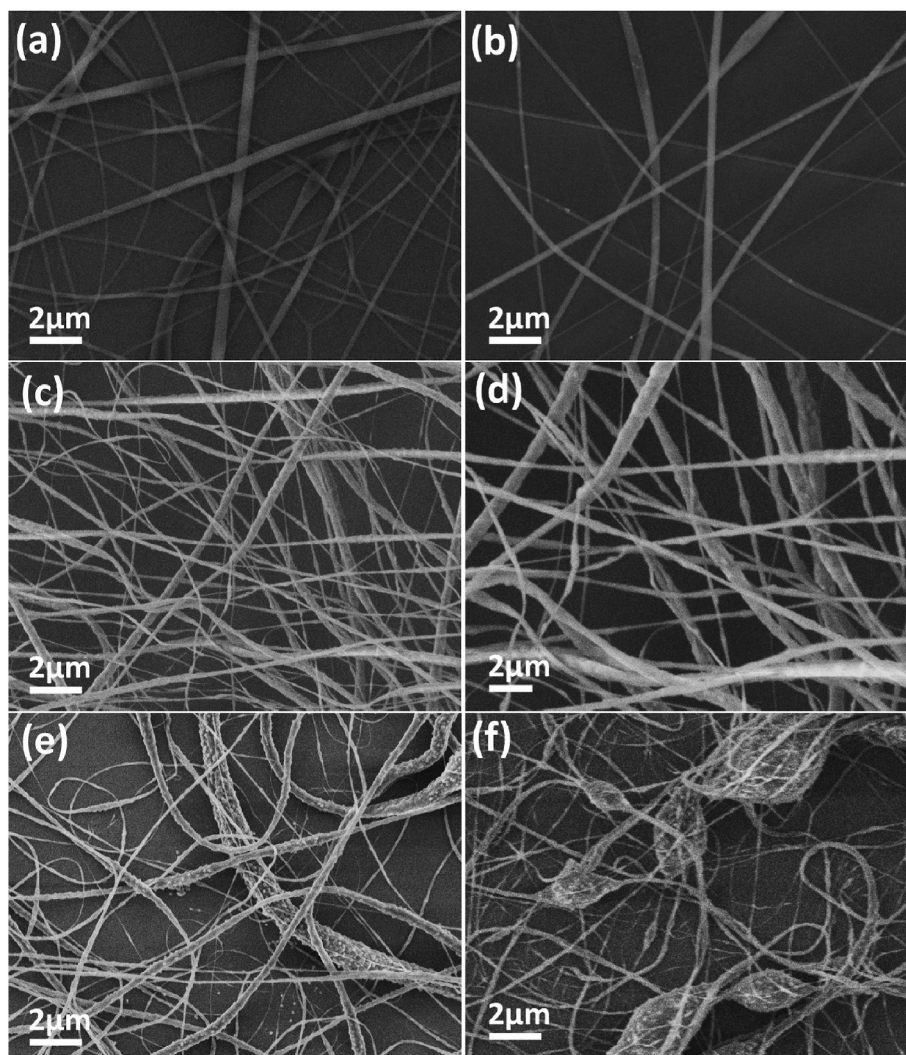


Fig. 1. SEM images of PVDF/KBT nanofibers with varying KBT content: (a) 0 wt%, (b) 2 wt%, (c) 5 wt%, (d) 7 wt%, (e) 10 wt%, and (f) 15 wt%.

doping concentration is evident through the heightened surface roughness of the nanofibers. Notably, the uniform distribution of filler particles within the composite fibres signifies a robust interfacial interaction between the PVDF polymer and the KBT materials. This strong interaction is expected to significantly amplify the piezoelectric characteristics of the composite. However, at doping levels of 10% and 15%, certain KBT nanoparticles exhibited limited dispersion within the PVDF nanofibers, leading to the agglomeration of the filler particles and the formation of large clumps with sizes reaching 5 μm after the electrospinning process. Therefore, the optimal doping ratio for KBT in PVDF lies within the range of 5% and 7%. SEM imaging elucidates the evolving morphology of the composite fibres, underlining the critical role of doping content in influencing both structural characteristics and potential piezoelectric performance enhancements.

Fig. 2 presents the results of X-ray diffraction (XRD) analysis conducted to investigate the crystallisation behaviour and phase composition of the PVDF/KBT composite. In Fig. 2a, the XRD spectra of PVDF/KBT composite fibres with varying KBT dopant levels are displayed. The peaks observed at 22.9° , 32.2° , 39.7° , 46.7° , and 57.2° correspond to the crystal planes of KBT [25]. The XRD pattern of KBT nanoparticles, shown in Fig. S1b, is consistent with the reported PDF card no. 04-022-2456. PVDF, a semi-crystalline polymer, comprises multiple phases, as evidenced by distinct peaks in the spectrum. A peak observed at 18.8° is attributed to the α phase, and two peaks at 19.2° and 39.5° correspond to (002) and (211) planes, respectively, indicating the presence of the semi-electroactive γ -crystalline phase. Additional peaks at 20.8° and 36.5° are associated with the (110/200) and (020) planes, respectively, representing the crystallisation of PVDF in the β -phase [26]. A nonlinear correlation is observed between the intensity of the β -phase peaks and the KBT content, suggesting an optimal doping rate for enhanced β -phase formation. The presence of KBT nanoparticles within PVDF/KBT nanofibers promotes PVDF orientation in β and γ phases, facilitated by interaction involving negatively charged KBT and dipolar moments of PVDF chains, driven by electrostatic forces and potential hydrogen bonding [27–29].

The crystallinity of PVDF/KBT nanofibers with different amounts of KBT filler was assessed using XRD patterns and the curve deconvolution analysis with Smartlab Studio II software (Fig. S2). The degree of crystallinity (DoC) and β -phase content in the composite fibres were determined based on the KBT content, as shown in Fig. 2b. The DoC values of PVDF/KBT composites displayed a dependency on the KBT doping percentage, reaching a peak value of 77.4%, approximately 1.19 times higher than pure PVDF nanofibers. The crystallinity of the β -phase exhibited significant variation as the KBT content varied in the PVDF/KBT composite, as observed through XRD patterns and curve deconvolution analysis. Notably, the PVDF/KBT composite containing 5 wt% KBT exhibited the highest percentage ($\sim 67\%$) of the β -PVDF phase. This enhanced β -phase content in PVDF/KBT could be attributed to the interactions between KBT particles and PVDF at the interfaces. However, in the case of the 15% KBT doping sample, a reduction in the β -phase

was observed, possibly due to the agglomeration of KBT particles within the PVDF matrix. Subsequent analysis and characterisation of the 5% KBT-doped PVDF/KBT sample were conducted using other techniques, such as Raman spectroscopy and AFM, to elucidate the effect of KBT nanoparticles on the crystal structure, as well as the local mechanical and piezoelectric response of the composite PVDF/KBT nanofiber at both the macroscopic and nanoscopic scales.

In order to further investigate the influence of the KBT filler on the proportion of the β phase, Raman mapping analyses were conducted on individual composite fibres. Fig. 3 presents the Nano-Raman spectroscopic measurements correlated with AFM of the nanocomposite fibres containing 5 wt% KBT nanoparticle content. In this study, surface-enhanced Raman scattering (SERS) measurements were performed, with the laser focal spot aligned at the centre of the AFM tip to ensure symmetrical scattering. Initially, the AFM non-contact mode was employed to locate a single fibre measuring $3 \times 3 \mu\text{m}^2$. Subsequently, SERS spectra were acquired from six positions on the AFM topographical image, labelled A to F. All spectra were obtained using the 300 nm laser focal diameter with 50 μW of 532 nm excitation laser and an accumulation time of 2 s. The observed Raman peaks at 890 and 1430 cm^{-1} corresponded to all three phases (α , β , and γ), while the peaks at 794 and 839 cm^{-1} were specifically attributed to the α phase and β phase, respectively [30]. Notably, peaks at 794, 839, 890, and 1430 cm^{-1} were evident in all spectra from the six positions. However, the incorporation of KBT nanoparticles induced distinct crystallisation behaviour in the PVDF material. A comparison was made between the Raman spectra of pure PVDF regions (A, B, C, F) and PVDF layers directly on top of the KBT fillers (position E), as indicated in the AFM topographical image. It is evident that the peaks exhibited lower intensity in the spectra of the pure PVDF regions, and only PVDF phases were discernible. In contrast, the spectra from position E, with embedded KBT nanoparticles, displayed sharper and more distinct peaks. The increased intensity of all Raman peaks confirmed that the presence of KBT particles enhanced the crystallisation of PVDF.

Furthermore, the incorporation of KBT particles facilitates crystallisation of the β -phase rather than the α -phase, as indicated by the heightened intensities of Raman peaks at 839 and 1430 cm^{-1} . Similar instances of β -phase formation in the presence of other fillers, such as organically modified clays like lead zirconate titanate (PZT) [31] or nanoparticles of ferrite materials [32], have been reported. The chemical composition and size of the nanoparticles play a critical role in promoting β -phase nucleation in PVDF. The introduction of KBT particles augments the crystallisation of the PVDF matrix in the form of the β -phase by acting as effective nucleating agents. In a PVDF/DMF solution, the interactions of C=O and $\text{CH}_2\text{-CF}_2$ dipoles involve robust dipolar interactions, potentially disrupting the $\text{C=O}\cdots\text{H-C}$ weak hydrogen bonding between the polymer chains, leading to PVDF dissolution [33]. These interactions also significantly influence PVDF crystallisation. The incorporation of ceramic KBT nanoparticles, serving as nucleating agents, likely strengthens hydrogen bonding ($\text{O-H}\cdots\text{F-C}$),

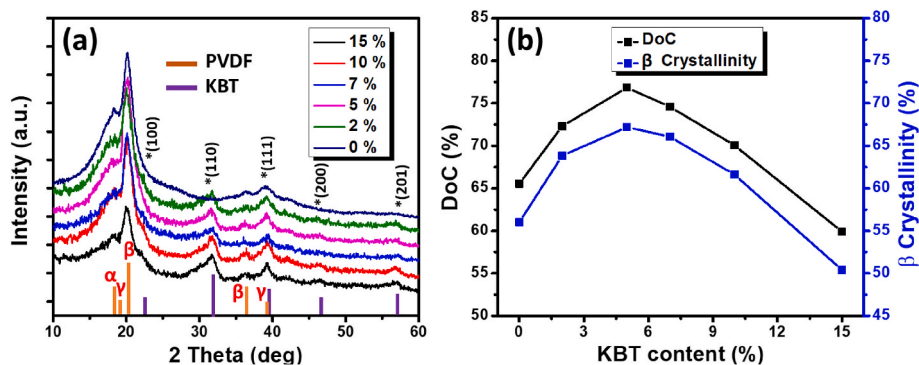


Fig. 2. (A) XRD patterns of PVDF/KBT nanofibers and (B) Influence of KBT filler content on the Degree of Crystallinity (DoC) and β -phase crystallinity.

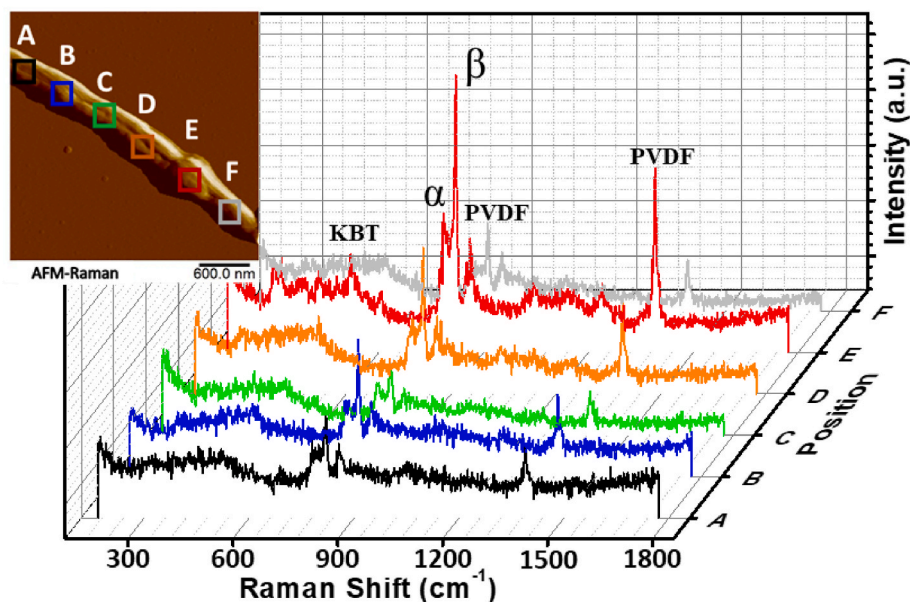


Fig. 3. AFM-correlated nano-Raman spectroscopy of a single PVDF/KBT nanofiber with corresponding SERS spectra taken from six positions on the nanofiber labelled from A to F.

promoting PVDF crystal nucleation. The increase in Coulombic forces or electrostatic repulsion at interfaces between KBT nanoparticles and PVDF, in conjunction with high electrical field poling during the electrospinning process, induces elongation and reorientation of the twisted PVDF chains along the fibres. This phenomenon promotes the local alignment of $\text{CH}_2\text{-CF}_2$ dipoles, which are packed in the TTTT configuration characteristic of the PVDF β -phase [20,34]. These findings collectively imply that the PVDF chains undergo a transformation into the electroactive β -phase through the incorporation of KBT and the electrospinning process.

3.2. Piezoelectric properties of PVDF/KBT nanofiber

The PVDF/KBT composite nanofibers exhibited an increased proportion of the β -phase, indicative of enhanced piezoelectric properties. To evaluate these properties, dual AC resonance tracking (DART) mode piezoresponse force microscopy (PFM) measurements were performed. Additionally, local hysteresis loops were acquired at various points on the PVDF/KBT nanofibers during the PFM measurements. In our study, PFM measurements were carried out in two stages. The first stage involved the poling process, wherein domains with opposite polarisation were induced by applying successive positive and negative DC voltages, known as the writing step. In this experiment, a poling bias of 30 V was selected, significantly larger than the coercive bias of PVDF. Subsequently, the resulting piezoelectric response of the sample was measured as the AC voltage of 3 V was swept, enabling the mapping of the piezoelectric response distribution across the sample surface, as depicted in Fig. 4. A PVDF/KBT nanofiber film on an ITO substrate with an area of $24 \times 24 \mu\text{m}^2$ was scanned. Fig. 4a illustrates the vertical amplitude response in PFM for the PVDF/KBT film with a poled area of $12 \times 12 \mu\text{m}^2$. Cross-sectional profile analysis in Fig. 4c indicates an average amplitude response of approximately 2000 p.m. The piezoresponse (PR) phase presents a clear contrast between the two domains in Fig. 4b. The PR phase displays a dark colour in the inner square due to successive poling steps. Bright colours correspond to domains with dipoles pointing upward, leading to an out-of-phase relationship with the driving frequency. Conversely, dark colours signify domains with dipoles pointing downward, resulting in an in-phase alignment with the driving frequency. The cross-sectional analysis (Fig. 4d) reveals a 180° phase shift between the unpoled and poled domains. To explore the

influence of KBT nanoparticles on the piezoresponse of hybrid PVDF/KBT nanofibers, a direct examination of the role of the nanofillers within the PVDF matrix is essential. However, conventional PFM imaging mode measurements were impeded by nanofiber damage caused by the high lateral force in the AFM contact mode. The use of stiff cantilevers was necessary to minimise electrostatic forces on the cantilever and prevent damage or displacement of PVDF nanofibers. Consequently, PFM measurements were conducted in the spectral mode to compare the piezoelectric activity between regions with and without embedded KBT. Initially, the tapping mode AFM was utilised to identify positions with embedded KBT nanoparticles, followed by PFM spectroscopy measurements using the DART-PFM interface. The AFM tip was positioned on selected locations to acquire the necessary measurements. Fig. 4e and f presents the amplitude and corresponding PFM phase images of the selected region ($1.5 \times 1.5 \mu\text{m}^2$) of a single PVDF/GO nanofiber, respectively. Fig. 4e displays a distinct piezoelectric contrast in the PFM amplitude image, which is caused by the difference in piezoelectricity of PVDF and KBT. In contrast, the PFM phase image in Fig. 4f clearly reveals a distinct colour contrast at the sites where the KBT nanoparticles are embedded, indicating that the KBT nanocrystals exhibit significantly higher piezoelectricity compared to the PVDF polymer. Previous research has emphasised challenges in conducting piezoelectric imaging on PVDF nanofibers, despite the orientation of the piezoelectric β -phase. However, the findings presented herein offer compelling evidence that domain switching can be achieved in PVDF/KBT composite nanofibers.

Furthermore, for a deeper understanding of the impact of the KBT filler on local hysteresis loops, the analysis of piezoelectric strain and ferroelectric switching was undertaken through the evaluation of PFM amplitude and phase loops, respectively. For this measurement, the influence of KBT nanoparticles on the local mechanical properties of the composite nanofibers was discerned to differentiate regions affected by the KBT nanoparticles from unaffected ones. The presence of the KBT nanoparticles delineates distinct zones within the composite nanofibers, each characterised by varying mechanical behaviours. Fig. 5 represents DMT (Derjaguin Muller Toporov model) modulus images (Fig. 5a), deformation images (Fig. 5b) of a single PVDF/KBT nanofiber subjected to an applied force of 90 nN in PFQNM measurements. The impact of KBT nanoparticles on the PVDF's mechanical properties becomes apparent in the non-uniform distribution of modulus and deformation across the nanofiber. Analysis along a profile line (Fig. 5c) revealed a

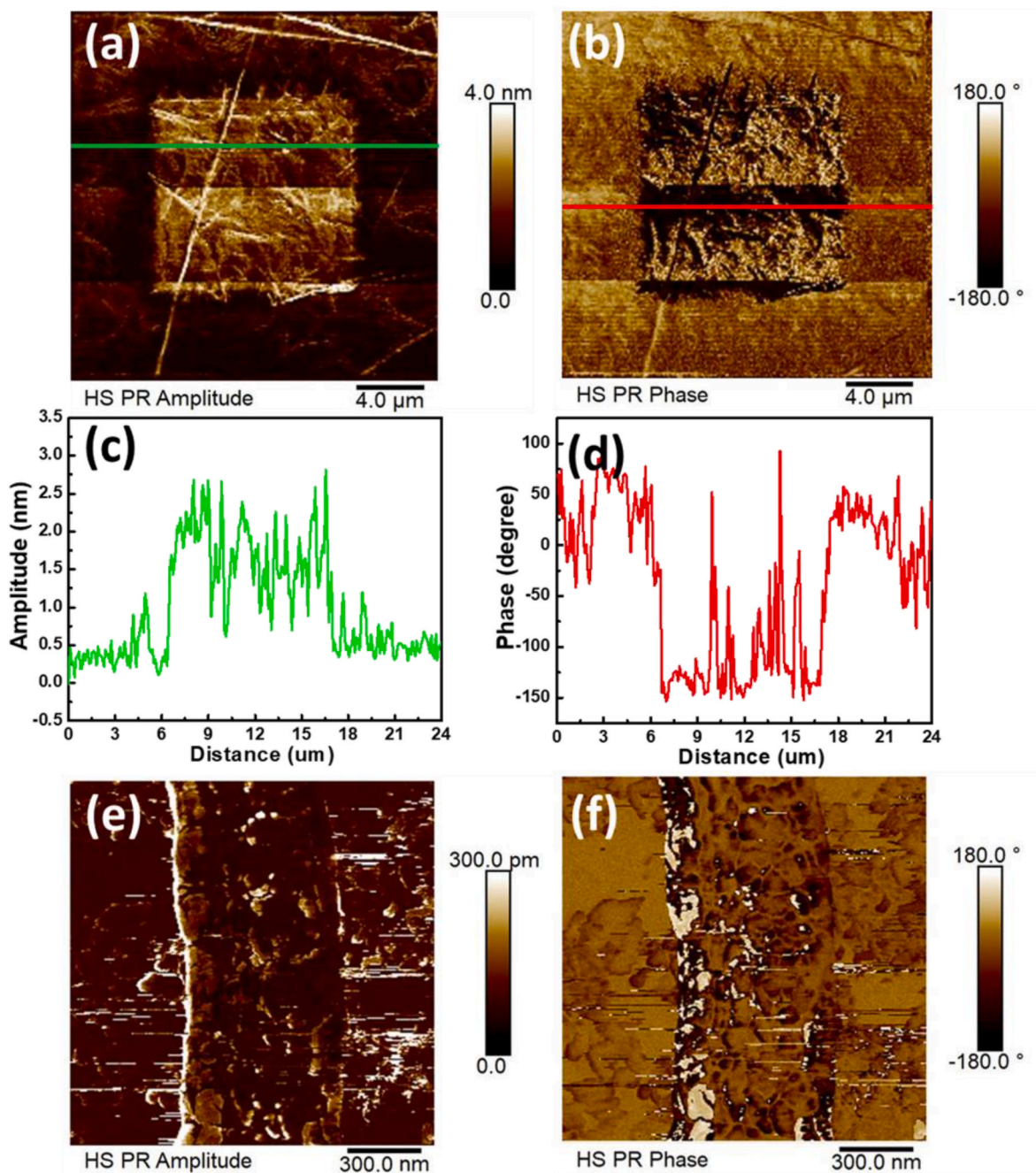


Fig. 4. Piezo-response characteristics of the PVDF/KBT nanofibers. (a) and (b) PFM amplitude and PFM phase images of poled PVDF/KBT nanofiber thin film showing domain switching upon applying 30 V to inner square, (c) and (d) Cross-sectional analysis of Amplitude and Phase (e) PFM amplitude and (f) PFM phase images of a portion of the single PVDF/KBT nanofiber revealing distribution of granular-type nanodomains with strong piezoelectric contrast.

significant rise in local modulus within the region containing embedded KBT nanoparticles (marked by the green circle), reaching approximately 4.5 GPa. In proximity to the nanoparticles, PVDF segments displayed a pronounced decrease in elastic modulus, leading to substantial deformation. Moving away from the nanoparticles, the polymeric matrix exhibited reduced stiffness, with the contact modulus diminishing from 4.5 GPa to 900 MPa, accompanied by a sharp rise in deformation values. Consequently, the inclusion of KBT nanoparticles elevates the nanofiber's impact resistance, with the polymer matrix bolstering nanoparticle immobilisation, thus substantially enhancing the composite's stability. Fig. 5d and e depict the PFM phase and amplitude loops from two regions within the PVDF/KBT nanofiber, designated by green and blue circles in Fig. 5b, representing areas with and without KBT

nanoparticles, respectively. Both PFM phase curves obtained from the PVDF and KBT-related positions display well-defined square-shaped 180° switching hysteresis loops with excellent repeatability. Remarkably, the nanocrystal structures remain undamaged during the sharp switching process induced by the electric field, making them highly suitable for electronic device applications. Nevertheless, a significant disparity in the coercive voltage (V_c) is discernible between the PVDF and KBT-related regions. The embedded KBT nanoparticles exhibit a negative switching bias of -8 V and a positive switching bias of $+12$ V, resulting in a final V_c of approximately 10 V. In contrast, the pure PVDF region exhibits a higher V_c , approximated at 15 V. It is noteworthy that the incorporation of KBT particles leads to a reduction in the coercive voltages. Additionally, the PR amplitude over the KBT region is

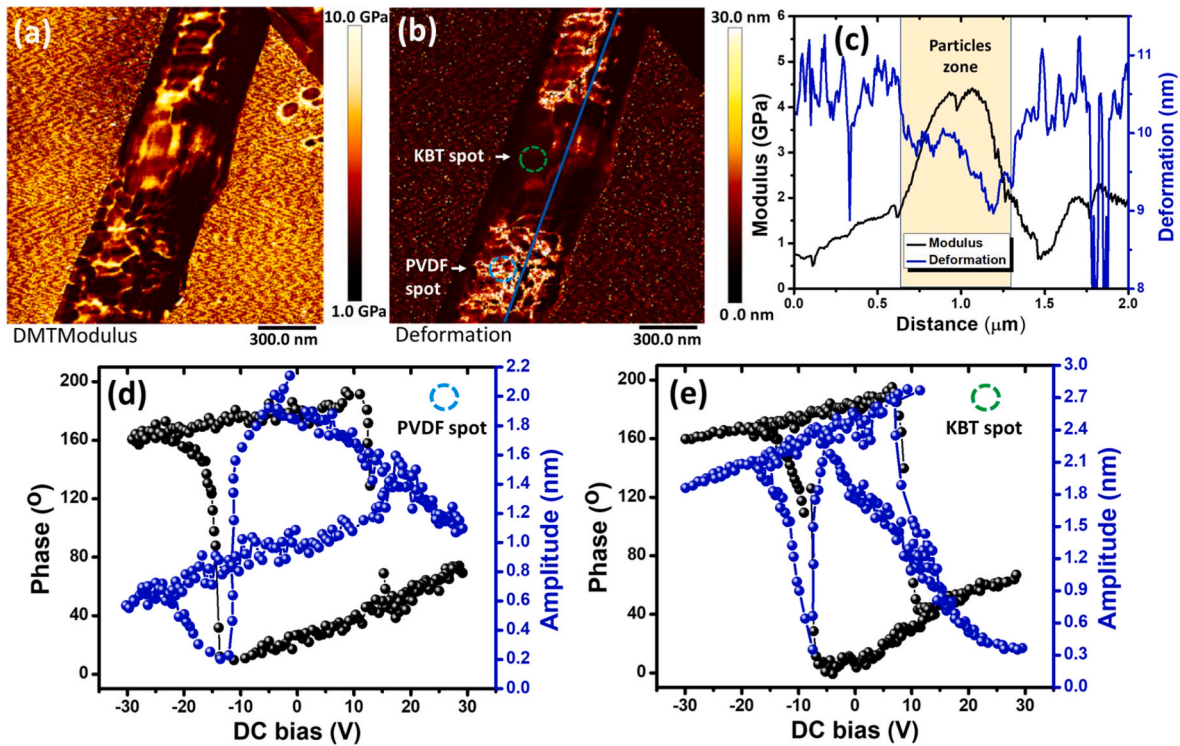


Fig. 5. (A) AFM modulus image, (b) deformation image and (c) line profile of the modulus and deformation along PVDF/KBT nanofibers. DART-PFM amplitude and phase responses corresponding to the locations marked as blue circle (d) correspond to the pure PVDF and green circle (e) correlates to embedded KBT nanoparticles. (For interpretation of the references to colour in this figure legend, the reader is referred to the Web version of this article.)

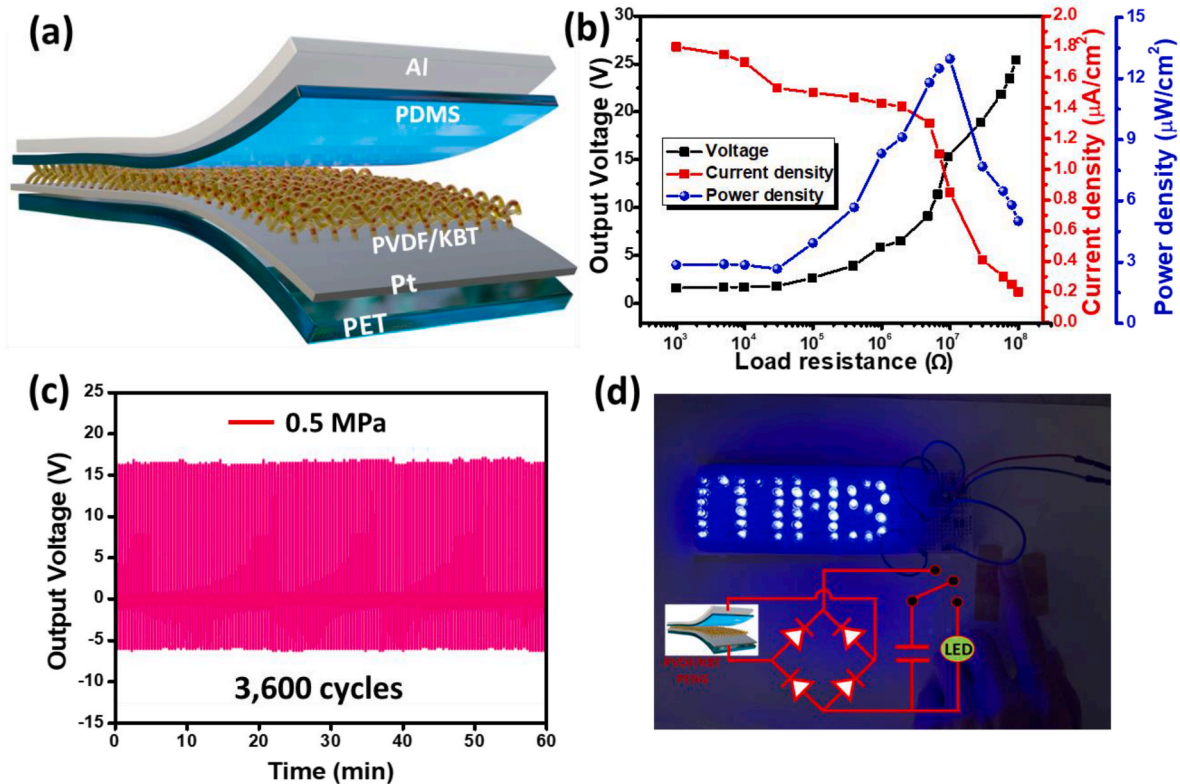


Fig. 6. (A) Schematic representation of the generator devices, (b) Variation of output voltage, current density, and power density of the PVDF/KBT nanofiber-based generator with respect to load resistance at an applied pressure/frequency of 0.5 MPa/1 Hz, (c) Mechanical endurance test of the generator measured continuously over 3600 cycles, (d) Powering of 43 commercial blue LEDs connected in an “ITIMS” configuration using the generated output power of the PVDF/KBT nanofiber-based generator under finger tapping. (For interpretation of the references to colour in this figure legend, the reader is referred to the Web version of this article.)

approximately 1.5 times higher than that of the pure PVDF regions, indicating an improved piezoelectric activity. Notably, the PVDF/KBT region exhibits distinctive butterfly-shaped amplitude versus Vdc (direct current voltage) loops (as indicated by the blue curve), with a peak amplitude of 2.7 nm achieved at Vdc = 10 V. These PFM findings establish that the incorporation of KBT nanoparticles enhances the piezoelectric and ferroelectric characteristics of the PVDF nanofibers. The piezoelectric constant d_{33} values for both the PVDF and KBT-related regions were determined using the following equation:

$$A = Q d_{33} V_{ac} \quad (3.1)$$

Where A is PFM amplitude, Q is the quality factor at contact resonance of the tip–sample, and V is the driving AC voltage applied to the tip. For the PVDF/KBT sample, the Q value was 30. Substituting these values into equation (3.1) yields a $d_{33} \sim 30$ p.m./V for the KBT spot and 21 p.m./V for the pure PVDF spot. Notably, the PVDF/KBT composite exhibits a higher d_{33} value compared to the pure PVDF, in alignment with the increased content and orientation of the polar phase observed through X-ray and Raman analysis. The enhanced piezoelectric properties of PVDF/KBT can be attributed not only to the high piezoelectricity of KBT but also to the presence of KBT particles, which engender the swelling of the PVDF chains and promote the formation of an extended β -phase conformation around them.

3.3. Energy harvesting ability of PVDF/KBT composite PEG

To evaluate the energy harvesting capability of the PVDF/KBT composite nanofibers, a piezoelectric generator (PEG) was constructed based on the device structure of PET/Pt/PVDF-KBT/PDMS/Al, as depicted in Fig. 6a. Two copper wires were affixed to the electrodes using conductive silver paste to establish electrical connections. The resultant PEG device was then safeguarded with antistatic tape. To assess the electrical performance of the PVDF/KBT nanofiber-based generator, experimental measurements were carried out employing a custom-designed mechanical pushing tester with a tapping area of 1 cm², as depicted in Fig. S3 and Video S1. The output voltage generated from the PEG was captured and recorded using an oscilloscope. The press-release mode was modulated by adjusting the applied force and frequency via customised PEG measurement software. In practical applications, piezoelectric devices are subjected to external loads. The output power of the PVDF/KBT nanofiber-based PEG is contingent upon external resistive loads. Consequently, we conducted measurements and computed the instantaneous output power density across various external load resistors spanning from 1 k Ω to 100 M Ω , as illustrated in Fig. 6b. Under a specific load resistance, the piezoelectric voltage response exhibits a characteristic peak voltage. This voltage is determined by accumulated piezoelectric charge. Charge enters the device due to mechanical strain and exits through the load resistance. Conversely, the piezoelectric charge experiences continuous leakage through the load resistance. As the load resistance is increased, the peak voltage escalates until it approximates the ideal open-circuit voltage limit, illustrated by the black curve in Fig. 6b. Furthermore, the peak voltage is subject to the force application frequency and the device's area. In contrast to the voltage, which rises monotonically with increasing load resistance, and the current, which declines monotonically, the power, denoting the product of current and voltage, reaches a maximum at a specific load resistance commonly referred to as the optimum load resistance or matching resistance as represented by the blue curve in Fig. 6b. At an applied pressure of 0.5 MPa and a frequency of 1 Hz, the peak instantaneous power density reached around 13.6 μ W/cm² with a load resistance of 10 M Ω . This achieved power density exceeds that of PEGs-based PVDF composites. Specifically, the PVDF/KBT nanofiber-based PEG exhibited a peak short-circuit current density and an open-circuit voltage of approximately 0.85 μ A/cm² and 16 V, respectively. The upward pushing amplitude and downward

releasing amplitude are illustrated in Fig. S4a. The voltage values from the PEG exhibited an increase as the applied pressure escalated, as shown in Fig. S4b. Furthermore, the PVDF/KBT nanofiber-based PEG exhibited consistent output amplitudes without depletion over 3600 continuous cycles at 0.5 MPa and 1 Hz, underscoring its exceptional mechanical robustness (Fig. 6c). In addition, the reliability of the device operation was assessed by charging a capacitor to power LEDs. Blue LEDs with a forward voltage of 3.35 V were utilised and connected in an ITIMS wiring configuration. The PEG output was rectified via a full-wave bridge rectifier, transforming the AC output into DC, which was subsequently connected to a 470 μ F capacitor in conjunction with an LED array, as elucidated in the circuit diagram outlining the capacitor-charging behaviour in Fig. 6d. With the capacitor reaching a maximum voltage of 50 V, a combination of series and parallel connections was used for the LEDs. Under the stimulus of hand tapping for 10 min, the generator effectively powered and illuminated approximately 43 LEDs, as verified by the snapshot presented in Fig. 6d and Video S2. These results unequivocally demonstrate the significant potential of the PVDF/KBT composite nanofiber-based piezoelectric generator as an eco-friendly power solution for powering wearable electronic devices.

4. Conclusions

In summary, this study adeptly employed the electrospinning process to manufacture PVDF/KBT nanofibers, yielding a substantial β -phase content of 67%. Employing nanoscale visualisation through AFM techniques, we revealed that the piezoelectric responses of the PVDF/KBT composite experienced significant enhancement, primarily attributed to the augmented orientation of the electroactive β -phase. This enhancement was effectively facilitated by the incorporation of KBT particles. Notably, the piezoelectric constant (d_{33}) value measured at the KBT particle zone of the PVDF/KBT composite fibre approximated 30 p.m./V, representing a 1.43-fold improvement compared to pure PVDF counterparts. Through optimisation of the KBT nanoparticle content within the PVDF matrix, the resultant PVDF/KBT composite fibre-based PEG achieved an impressive output power density of 13.6 μ W/cm². Noteworthy is the exceptional mechanical resilience of this PEG variant when the KBT content was 5 wt%. Moreover, the efficacy of the PEG was substantiated by swift capacitor charging and successful illumination of LEDs. In sum, this study unveils a viable approach to tailor PVDF composites, endowing them with adjustable mechanical and piezoelectric properties. This advancement holds promise in driving the evolution of self-charging power systems for wearable and portable electronic devices.

Declaration of competing interest

The authors declare that they have no known competing financial interests or personal relationships that could have appeared to influence the work reported in this paper.

The authors declare the following financial interests/personal relationships which may be considered as potential competing interests: Van-Dang Tran reports financial support was provided by Vietnam Ministry of Education and Training.

Acknowledgements

This work is funded by the Ministry of Education and Training (MOET), Vietnam under the project (No. B2022-BKA-13).

Appendix A. Supplementary data

Supplementary data to this article can be found online at <https://doi.org/10.1016/j.ceramint.2023.09.161>.

References

- [1] IEA, World Energy Outlook. <https://www.iea.org/reports/world-energy-outlook-2022>, 2022.
- [2] F.R. Fan, W. Tang, Z.L. Wang, Flexible nanogenerators for energy harvesting and self-powered electronics, *Adv. Mater.* 28 (2016) 4283–4305, <https://doi.org/10.1002/adma.201504299>.
- [3] C.R. Bowen, H.A. Kim, P.M. Weaver, S. Dunn, Piezoelectric and ferroelectric materials and structures for energy harvesting applications, *Energy Environ. Sci.* 7 (1) (2014) 25–44, <https://doi.org/10.1039/C3EE42454E>.
- [4] H. Liu, J. Zhong, C. Lee, S.W. Lee, L. Lin, A comprehensive review on piezoelectric energy harvesting technology: materials, mechanisms, and applications, *Appl. Phys. Rev.* 5 (4) (2018), 041306, <https://doi.org/10.1063/1.5074184>.
- [5] D. Hu, M. Yao, Y. Fan, C. Ma, M. Fan, M. Liu, Strategies to achieve high performance piezoelectric nanogenerators, *Nano Energy* 55 (2019) 288–304, <https://doi.org/10.1016/j.nanoen.2018.10.053>.
- [6] C. Covaci, A. Gontean, Piezoelectric energy harvesting solutions: a review, *Sensors* 20 (2020) 3512, <https://doi.org/10.3390/s20123512>.
- [7] X. Lin, X. Zhang, X. Fei, C. Wang, H. Liu, S. Huang, Flexible three-dimensional interconnected PZT skeleton based piezoelectric nanogenerator for energy harvesting, *Ceram. Int.* 16 (2023) 27526–27534, <https://doi.org/10.1016/j.ceramint.2023.06.028>.
- [8] S. Banerjee, S. Bairagi, S.W. Ali, A critical review on lead-free hybrid materials for next generation piezoelectric energy harvesting and conversion, *Ceram. Int.* 12 (2021) 16402–16421, <https://doi.org/10.1016/j.ceramint.2021.03.054>.
- [9] S. Veeralingam, S. Badhulika, Lead-free transparent flexible piezoelectric nanogenerator for self-powered wearable electronic sensors and energy harvesting through rainwater, *ACS Appl. Energy Mater.* 5 (2022) 12884–12896, <https://doi.org/10.1021/acsaem.2c02521>.
- [10] L. Qiao, G. Li, H. Tao, J. Wu, Z. Xu, F. Li, Full characterization for material constants of a promising KNN-based lead-free piezoelectric ceramic, *Ceram. Int.* 46 (2020) 5641–5644, <https://doi.org/10.1016/j.ceramint.2019.11.009>.
- [11] S. Sukumaran, S. Chatbourni, D. Rouxel, E. Tisserand, F. Thiebaud, T. Ben Zineb, Recent advances in flexible PVDF based piezoelectric polymer devices for energy harvesting applications, *J. Intell. Mater. Syst. Struct.* 32 (7) (2021) 746–780, <https://doi.org/10.1177/1045389X20966058>.
- [12] J. Li, G. Zhou, Y. Hong, W. He, S. Wang, Y. Chen, C. Wang, Y. Tang, Y. Sun, Y. Zhu, Highly sensitive, flexible and wearable piezoelectric motion sensor based on PT promoted-phase PVDF, *Sens. Actuators Phys.* 337 (2022), 113415, <https://doi.org/10.1016/j.sna.2022.113415>.
- [13] W. Wu, S. Bai, M.M. Yuan, Y. Quin, Z.L. Wang, Wang, T. Jing, Lead zirconate titanate nanowire textile nanogenerator for wearable energy-harvesting and self-powered devices, *ACS Nano* 6 (2012) 6231–6235, <https://doi.org/10.1021/nn3016585>.
- [14] S. Swathy, S. Panicker, S.P. Rajeev, V. Thomas, Impact of PVDF and its copolymer-based nanocomposites for flexible and wearable energy harvesters, *Nano-Struct. & Nano-Objects* 34 (2023), 100949, <https://doi.org/10.1016/j.nanoso.2023.100949>.
- [15] R. Hasegawa, Y. Takahashi, Y. Chatani, Crystal structures of three crystalline forms of poly(vinylidene fluoride), *Polym. J.* 3 (1972) 600–610, <https://doi.org/10.1295/polymj.3.600>.
- [16] X. Liu, S. Xu, X. Kuang, X. Wang, Ultra-long MWCNTs highly oriented in electrospun PVDF/MWCNT composite nanofibers with enhanced β phase, *RSC Adv.* 6 (2016) 106690–106696, <https://doi.org/10.1039/C6RA24195F>.
- [17] L. Parali, M. Koç, E. Akça, Fabrication and Characterization of High Performance PVDF-based flexible piezoelectric nanogenerators using PMN-xPT (x:30, 32.5, and 35) particles, *Ceram. Int.* 11 (2023) 18388–18396, <https://doi.org/10.1016/j.ceramint.2023.02.211>.
- [18] T. Umasankar Patro, Milind V. Mhalgi, D.V. Khakhar, Ashok Misra, Studies on poly (vinylidene fluoride)–clay nanocomposites: effect of different clay modifiers, *Polymer* 49 (2008) 3486–3499, <https://doi.org/10.1016/j.polymer.2008.05.034>.
- [19] J.E. Lee, Y. Eom, Y.E. Shin, S.H. Hwang, H. Ko, H.G. Chae, Effect of interfacial interaction on the conformational variation of poly(vinylidene fluoride) (PVDF) chains in PVDF/graphene oxide (GO) nanocomposite fibers and corresponding mechanical properties, *ACS Appl. Mater. Interfaces* 11 (2019) 13665–13675, <https://doi.org/10.1021/acsaami.8b22586>.
- [20] X. Liu, J. Ma, X. Wu, L. Lin, X. Wang, Polymeric nanofibers with ultrahigh piezoelectricity via self-orientation of nanocrystals, *ACS Nano* 11 (2017) 1901–1910, <https://doi.org/10.1021/acsnano.6b07961>.
- [21] Y. Wei, N. Zhang, C. Jin, W. Zhu, Y. Zeng, G. Xu, L. Gao, Z. Jian, *Bi_{0.5}K_{0.5}TiO₃-CaTiO₃ ceramics: appearance of the pseudocubic structure and ferroelectric-relaxor transition characters*, *J. Am. Ceram. Soc.* 102 (2019) 3598–3608, <https://doi.org/10.1111/jace.16244>.
- [22] I. Krad, O. Bidault, N. Geoffroy, M. El Maaoui, Preparation and characterization of K_{0.5}Bi_{0.5}TiO₃ particles synthesized by a stirring hydrothermal method, *Ceram. Int.* 3 (2016) 3751–3756, <https://doi.org/10.1016/j.ceramint.2015.10.158>.
- [23] Y. Hou, M. Zhu, L. Hou, J. Liu, J. Tang, H. Wang, H. Yan, *Synthesis and characterization of lead-free K_{0.5}Bi_{0.5}TiO₃ ferroelectrics by sol-gel technique*, *J. Cryst. Growth* 273 (2005) 500–503, <https://doi.org/10.1016/j.jcrysgro.2004.09.055>.
- [24] N.T. Cuong, S. Barrau, M. Dufay, N. Tabary, A. Da Costa, A. Ferri, R. Lazzaroni, J. M. Raquez, P. Leclère, On the nanoscale mapping of the mechanical and piezoelectric properties of poly (L-Lactic acid) electrospun nanofibers, *Appl. Sci.* 10 (2020) 652, <https://doi.org/10.3390/app1002065>.
- [25] M. Badole, S. Dwivedi, T. Pareek, S.A. Ahmed, S. Kumar, *Significantly improved dielectric and piezoelectric properties of BiAlO₃ modified potassium bismuth titanate lead-free ceramics*, *Mater. Sci. Eng. B* 262 (2020), 114749, <https://doi.org/10.1016/j.mseb.2020.114749>.
- [26] I.Y. Abdullah, M. Yahaya, M.H.H. Jumali, H.M. Shanshool, Effect of annealing process on the phase formation in poly(vinylidene fluoride) thinfilms, *AIP Conf. Proc.* 1614 (2014) 147, <https://doi.org/10.1063/1.4895187>.
- [27] S. Dwivedi, M. Badole, T. Pareek, S. Kumar, *Multifunctional lead-free K_{0.5}Bi_{0.5}TiO₃-based ceramic reinforced PVDF matrix composites*, *J. Alloys Compd.* 871 (2021), 159616, <https://doi.org/10.1016/j.jallcom.2021.159616>.
- [28] H. Hong, S.A. Song, S.S. Kim, *Phase transformation of poly (vinylidene fluoride)/TiO₂ nanocomposite film prepared by microwave-assisted solvent evaporation: an experimental and molecular dynamics study*, *Compos. Sci. Technol.* 199 (2020), 108375, <https://doi.org/10.1016/j.compscitech.2020.108375>.
- [29] A. Gaur, R. Shukla, B. Kumar, A. Pal, S. Chatterji, R. Ranjan, P. Maiti, Processing and nanoclay induced piezoelectricity in poly(vinylidene fluoride-co-hexafluoro propylene) nanohybrid for device application, *Polymer* 97 (2016) 362–369, <https://doi.org/10.1016/j.polymer.2016.05.049>.
- [30] C.J. Constantino, A.E. Job, R.D. Simões, J.A. Giacometti, V. Zucolotto, O. N. Oliveira, G. Gozzi, D.L. Chinaglia, Phase transition in poly(vinylidene fluoride) investigated with micro-Raman spectroscopy, *Appl. Spectrosc.* 59 (2005) 275–279, <https://doi.org/10.1366/0003702053585336>.
- [31] T. Greeshma, R. Balaji, J. S. PVDF phase formation and its influence on electrical and structural properties of PZT-PVDF composites, *Ferroelectr. Lett.* 40 (2013) 41–55, <https://doi.org/10.1080/07315171.2013.814460>.
- [32] S. Jiang, H. Wan, H. Liu, Y. Zeng, J. Liu, Y. Wu, G. Zhang, *High β phase content in PVDF/CoFe₂O₄ nanocomposites induced by DC magnetic fields*, *Appl. Phys. Lett.* 109 (2016), 102904, <https://doi.org/10.1063/1.4962489>.
- [33] R.K. Singh, S.W. Lye, J. Miao, Holistic investigation of the electrospinning parameters for high percentage of β -phase in PVDF nanofibers, *Polymer* 214 (2021), 123366, <https://doi.org/10.1016/j.polymer.2020.123366>.
- [34] S. Mondal, T. Paul, S. Maiti, B.K. Das, K.K. Chattopadhyay, Human motion interactive mechanical energy harvester based on all inorganic perovskite-PVDF, *Nano Energy* 74 (2020), 104870, <https://doi.org/10.1016/j.nanoen.2020.104870>.